



## Article

# The Impact of Offshore Wind Farms on Sea State Demonstrated by Airborne LiDAR Measurements

Konrad Bärfuss <sup>1,\*</sup> , Johannes Schulz-Stellenfleth <sup>2</sup>  and Astrid Lampert <sup>1</sup> <sup>1</sup> Institute of Flight Guidance, Technische Universität Braunschweig, 38108 Braunschweig, Germany; astrid.lampert@tu-braunschweig.de<sup>2</sup> Helmholtz-Zentrum Hereon, Institute of Coastal Systems-Analysis and Modeling, 21502 Geesthacht, Germany; johannes.schulz-stellenfleth@hereon.de

\* Correspondence: k.baerfuss@tu-braunschweig.de

**Abstract:** The increasing number of wind farms installed in the North Sea has an impact on the downstream wind speed. This has been hypothesized as well for sea state properties. Wave effects can be expected in particular in fetch-limited conditions with offshore wind directions. With systematic flights deploying an airborne laser scanner, these impacts are shown directly for the first time. The flights were conducted perpendicular to the main wind direction upstream and downstream of the cluster of the offshore wind parks Amrumbank West, Nordsee Ost, and Meerwind Süd/Ost. The flight legs covered the area potentially influenced by the wind parks and the undisturbed area next to the wind parks. The analysis of the spectral energy distribution shows a re-distribution of the wave energy in the downstream area with enhanced energy at smaller wavelengths. The effect is still clearly visible at a distance of 55 km. As the sea surface constitutes the link between the atmosphere and the ocean, it is very likely that wind parks modify the properties of the water column as well.



**Citation:** Bärfuss, K.; Schulz-Stellenfleth, J.; Lampert, A. The Impact of Offshore Wind Farms on Sea State Demonstrated by Airborne LiDAR Measurements. *J. Mar. Sci. Eng.* **2021**, *9*, 644. <https://doi.org/10.3390/jmse9060644>

Academic Editor: Francesca De Serio

Received: 4 May 2021

Accepted: 6 June 2021

Published: 10 June 2021

**Publisher's Note:** MDPI stays neutral with regard to jurisdictional claims in published maps and institutional affiliations.



**Copyright:** © 2021 by the authors. Licensee MDPI, Basel, Switzerland. This article is an open access article distributed under the terms and conditions of the Creative Commons Attribution (CC BY) license (<https://creativecommons.org/licenses/by/4.0/>).

**Keywords:** oceanographic techniques; sea coast; sea measurements; sea surface; waves; wind farm; wake; LiDAR; laser scanner

## 1. Introduction

Renewable energies play a key role in the transition to climate neutral power supply. Wind energy contributes an increasing amount to the German energy sector. In particular, offshore wind power capacity will be expanded in the near future. In comparison to onshore wind parks, offshore wind parks provide the advantage of a location characterised by a higher average wind speed and better acceptance by the population. By the end of 2019, a total capacity of about 7.5 GW of offshore wind parks were operational, and the expected future commissioning exceeds 20 GW by 2030 [1].

It has been shown that wind parks can have long-range effects on the wind field for particular atmospheric conditions [2–4]. For stable atmospheric conditions, e.g., a temperature inversion induced by the flow of warm air masses from land above colder air masses influenced by the water surface, reduced wind speed in the downstream area has been reported to an extent of several 10 km [5].

In the project WInd Park Far Field (WIPAFF), 41 measurement flights were performed under different atmospheric conditions [6,7]. For a stably stratified atmosphere, the wind speed was typically reduced to around 75% directly downstream of the wind parks (so-called wake), and the recovery to 95% of the undisturbed flow took typically around 50 km [8]. For comparison, the wind speed was only reduced to 85% or less for turbulent mixing, and the recovery to 95% was typically accomplished within less than 15 km [8]. These measurement data were used for validation of numerical simulations with the Weather Research and Forecast Model (WRF), e.g., [9–11].

During the project WIPAFF, an airborne laser scanner was used to determine the surface parameters, which was used to link to satellite observations with synthetic aperture

radar (SAR). In parallel to the reduction of wind speed in the downstream wake, changes of the backscattered laser scanner signals were observed: an enhanced reflectance [12] and a reduced number of backscattered laser pulses.

At first glance, this indicates a lower roughness of the sea surface, where less side-ward laser pulses are backscattered and lost for the detection; however, the backscattered pulses contain more energy as the specular reflection is of higher probability at the less inclined surfaces. The laser scanner provides high resolution maps of the sea surface elevation, which can be used to analyse three-dimensional ocean wave fields and the associated spectra.

The WIPAFF data set of an airborne laser scanner was used to derive the significant wave height for all flights. Very good agreement was found for the comparison with buoy data during overpasses [13]. The significant wave height was further compared to the results of a wave model (WAM). Good agreement was found for large water depths. However, in particular in coastal areas with shallow bathymetry, the WAM underestimated the significant wave height [13].

To further investigate the interaction of large-scale wakes of different wind parks and wind park clusters and the modifications of the wind field for flow above the coast, currently, the project X-Wakes addresses these questions with a combination of extensive measurements and numerical simulations. Although the focus is on atmospheric measurements and simulations, satellite-based products of large-scale wind field modifications are used as in WIPAFF, where the algorithm is based on analysing the sea surface roughness, which modifies radar backscatter. Again, the aircraft is used as a link between the analysis of surface properties (laser scanner and surface temperature) and atmospheric properties by in-situ measurements.

Local and regional changes of the sea state have different implications. Offshore work is limited by wave properties. E.g., maintenance work at wind turbines from ships is typically possible up to a significant wave height of about 2 m [14]. A different wind wave climate further has an influence on the circulation [15], and the surface couples back into the atmosphere [16].

As wind is the key driver of wave development, the impact of changes in the wind field on the sea state is clear. The atmosphere and sea are coupled via the surface, and therefore properties modifying the sea surface are highly relevant for processes taking place in the water body as well.

As a consequence, the wind wake of offshore wind farms generates an oceanic response and alters the upper ocean circulation, with the intensity depending on the wind wake's extension compared to the internal Rossby radius of deformation [17]. The associated change in the ocean upwelling and modification of the pycnocline is shown in [18]. The changes to the water turbulence and stratification in addition to changes in the flow and salinity distribution therefore ultimately impact the biogeochemical processes and the food web, e.g., [19] and the references therein.

One might expect an influence of offshore wind farm structures on the sea state. This has been studied in simulations by [20,21]. The latter considered the additional effect of a reduced friction velocity inside the offshore wind farms. Both found that wave dissipation and reflection/diffraction on structures affected the significant wave height locally. The reduced friction velocity, however, modified the significant wave height at 15 km behind the wind farm and beyond.

This article investigates, in detail, the modifications of sea state downstream of wind parks. Section 2 introduces the theory of wave development and, in particular, the spectral energy distribution for increasing fetch length. In Section 3, the airborne laser scanner system and the data processing to derive sea state spectral properties are described. Section 4 describes the meteorological and environmental conditions on 8 August 2017, which is used as a case study for analysing the changes of the sea state in Section 5. Here, the wave properties and energy distribution in the spectral range for areas affected by the influence of wind parks are compared to areas that undergo the natural development of sea state

with increasing fetch. The article concludes with the discussion of a broader range of potential implications of the results in Section 6.

## 2. Basic Wave Dynamics

The waves observed in this study are so-called surface gravity waves. These waves are generated by the wind and can have wavelengths of up to several hundred meters with periods up to about 20 s. When the wind starts to blow over a smooth ocean surface, it generates shorter waves at the beginning, which subsequently grow in length and period due to nonlinear interactions inside the two-dimensional wave spectrum  $F$ . The evolution of the wave spectrum can be described by the so-called wave action balance equation [22]

$$\frac{\partial N}{\partial t} + \nabla \cdot c_g N = S_{wind} + S_{diss} + S_{nonl}. \quad (1)$$

Here,  $N = F/\omega$  is the wave action with wave frequency  $\omega$ ,  $c_g$  is the wave group velocity, and  $S_{wind}$ ,  $S_{diss}$ , and  $S_{nonl}$  are source functions describing the wind generation, the dissipation, and the nonlinear coupling of waves. The action balance equation is the basis for the state-of-the-art wave models run at various weather centres around the world. The nonlinear interaction component is the only part of the model that can be derived from first-order physics principles thus far. Both dissipation and wind generation source functions contain empirical components, which were tuned to observations.

In fetch-limited conditions as present during the observations discussed in this study, most of the energy input from the wind is absorbed by the spectral region around the peak of the wave spectrum. This energy is then moved by nonlinear processes both to longer and shorter waves. The energy transport to shorter waves eventually leads to wave dissipation, e.g., due to wave breaking. The energy flux toward longer wavelengths produces the so-called swell, which can propagate over long distances. Exemplaric wave spectra for different fetch lengths and wind speeds are shown in Figure 1.

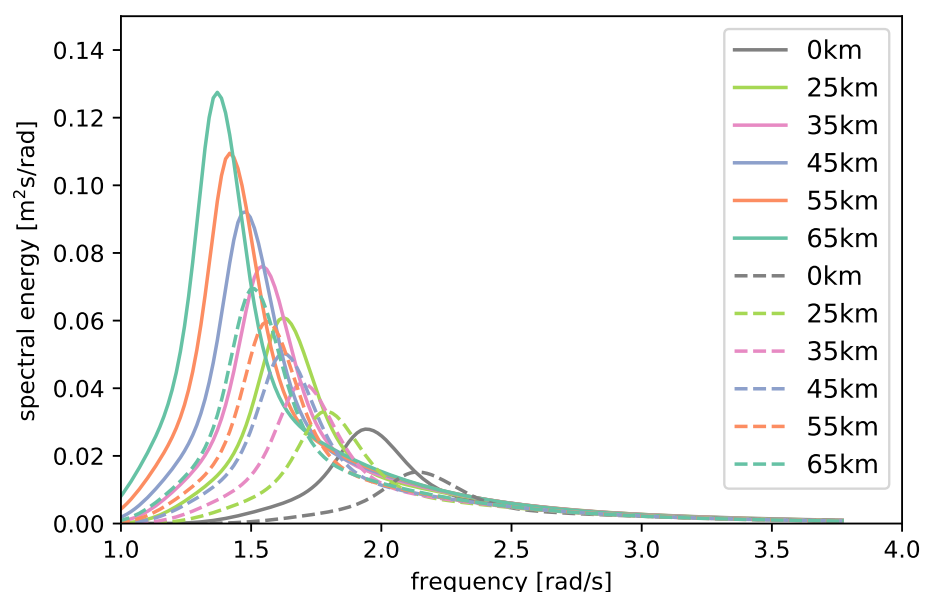


**Figure 1.** JONSWAP spectra for different distances to the wind farm and wind speeds of  $4 \text{ m s}^{-1}$  (solid lines) and  $3 \text{ m s}^{-1}$  (dashed lines). At 80 km, fetch wave heights of about 0.8 m for  $4 \text{ m s}^{-1}$  and 0.6 m for  $3 \text{ m s}^{-1}$  are found. The JONSWAP shape parameters were chosen as  $\gamma = 3.3$ ,  $\sigma_a = 0.07$ , and  $\sigma_b = 0.09$ .

## 3. Techniques to Retrieve Spectral Data

An airborne LiDAR (RIEGL VZ-1000, Riegl GmbH, Austria) was implemented in the research aircraft Dornier 128 D-IBUF of TU Braunschweig (Germany) [23] to measure the

sea surface similar to the measurements in Reineman et al. [24], Walsh et al. [25], Melville et al. [26], Romero and Melville [27]. Combining the LiDAR's relative range and position data with a highly accurate INS system (presented in Schwithal et al. [28]) consisting of an iMAR RQH (iMAR GmbH, Germany) and a multi constellation GNSS receiver provides a geolocated elevation point cloud of the scanned sea surface.

The system and its measurements are introduced in Bärffuss et al. [13] and Lampert et al. [7], whereas datasets preprocessed for sea surface elevation variance are available in Bärffuss et al. [6]. In addition to processing the variance of the surface elevation measurements  $\eta$  to estimate the significant waveheight  $H_s \approx 4\sqrt{\text{var}(\eta)} = H_{m0}$ , the observed surface can be transformed into the spectral domain and, subsequently, into the directional sea surface variance density spectrum.

To observe the omnidirectional spectrum, the directional spectrum is integrated over all directions. The resulting one-dimensional variance density spectrum is a common representation of the sea state, which can also be obtained using in-situ techniques, such as wave buoy measurements [29] or wave pole measurements (e.g., [30]).

### 3.1. Subsampling and Aliasing

The LiDAR system detects less returns with high incident angles on the sea surface as the reflectance decreases (e.g., Otremba and Piskozub [31], Sayer et al. [32]) and, therefore, does not reflect enough laser pulse energy for the detector inside the laser scanner. This effect is illustrated in Reineman et al. [24]. In combination with the low flight altitude of 90–120 m above sea level during the measurement flights in the project WIPAFF [5,7,12], the surface elevation was sampled within a swath width of around 60–80 m, while the minimum point density reached  $1 \text{ m}^{-2}$ .

This resulted in subsampling below angular frequencies of around  $0.75 \text{ rad s}^{-1}$ . The omnidirectional spectrum shall not be taken into account below that frequency. At the other end, the Nyquist frequency [33] (the frequency at which energy in the upperside frequency bands is mirrored into the frequency bands below) was located around  $6 \text{ rad s}^{-1}$ . Regarding the high frequency tail of a typical sea surface spectrum with a slope in the range from  $w^{-4}$  to  $w^{-5}$ , aliasing errors are expected to be negligible.

### 3.2. Measuring the Sea Surface from a Moving Platform

Since the sea surface elevations for the computation of two dimensional spectra is not observed instantaneously for the case of a line scan pattern [34], the relative velocity between the phase speed of single wave components and the speed of the observing platform is distorted similar to the well-known Doppler-shift. The distortion is

$$\Delta k_{x,y} = k_{x,y} - k'_{x,y} \quad (2)$$

where  $k'_x, k'_y$  denote wavenumber components as observed from the moving platform. As Walsh et al. [35] indicated, the distortion along the ground track, which is aligned with the  $x$ -axis, is shown to be

$$\Delta k_x = \frac{\omega}{V_{G_x}} \quad (3)$$

with  $\omega$  as the angular frequency of the respective angular wavenumber  $k$ , and  $V_{G_x}$  as the ground speed of the carrier platform. The relation between  $\omega$  and  $k$  is given by the dispersion relation  $\omega^2 = gk \tanh kd$  (e.g., [36]), depending on the gravitational acceleration  $g$  and the water depth  $d$ . The correction of Equation (3) is usually applied to resolve the scanning distortion (e.g., [37,38]), whereas a more general discussion can be found in Long [39].

In the case of a relevant wind correction angle (WCA) and/or a misalignment  $\Theta$  of the line scan direction and the aircraft's body fixed  $y$ -direction according to international aerospace definitions (ISO 1151-2:1985), a virtual velocity  $V'_{G_y}$  between the scan line crossing

an Earth fixed  $y$ -axis normal to the aircraft's ground speed vector can be introduced. This crossing velocity is equal to

$$V'_{G_y} = \frac{V_{G_x}}{\tan(WCA + \Theta)} \quad (4)$$

and can be used to compute

$$\Delta k_y = \frac{\omega}{V'_{G_y}} \quad (5)$$

$$\Delta k_y = \omega \cdot \frac{\tan(WCA + \Theta)}{V_{G_x}} \quad (6)$$

similar to the computation of  $V_{G_x}$ . The observed sea surface components  $k_y$  are, therefore, not altered for small wind correction and misalignment angles. Although the process of resolving the distortion might be regarded as complex, Walsh et al. [35] indicated that ambiguous spectral peaks in line scan measurements can be resolved by measuring a statistically similar surface in different directions compared to instantaneous measurements (photogrammetry).

### 3.3. Discussion of the Subsequent Limitations

Low frequencies are affected the most by scanning distortion. At  $1 \text{ rad s}^{-1}$ , the distortion is around 10 percent, and at  $4 \text{ rad s}^{-1}$ , below 5 percent in wavenumbers. Therefore, the direction estimate degenerates toward low frequencies.

As more  $k$ -vectors (equally spaced in the  $x$ - and  $y$ -directions) are present for the convolution into an omnidirectional spectrum toward higher frequencies, the relative estimation error of the variance density estimate is reduced toward high frequencies according to [30] with

$$\sigma = 100\% \cdot N^{-0.5} \quad (7)$$

where  $N$  denotes the number of  $k$ -vectors for a specific omnidirectional wavenumber.

An exemplaric spectrum with a  $1\sigma$ -error regime is shown in Figure 2.

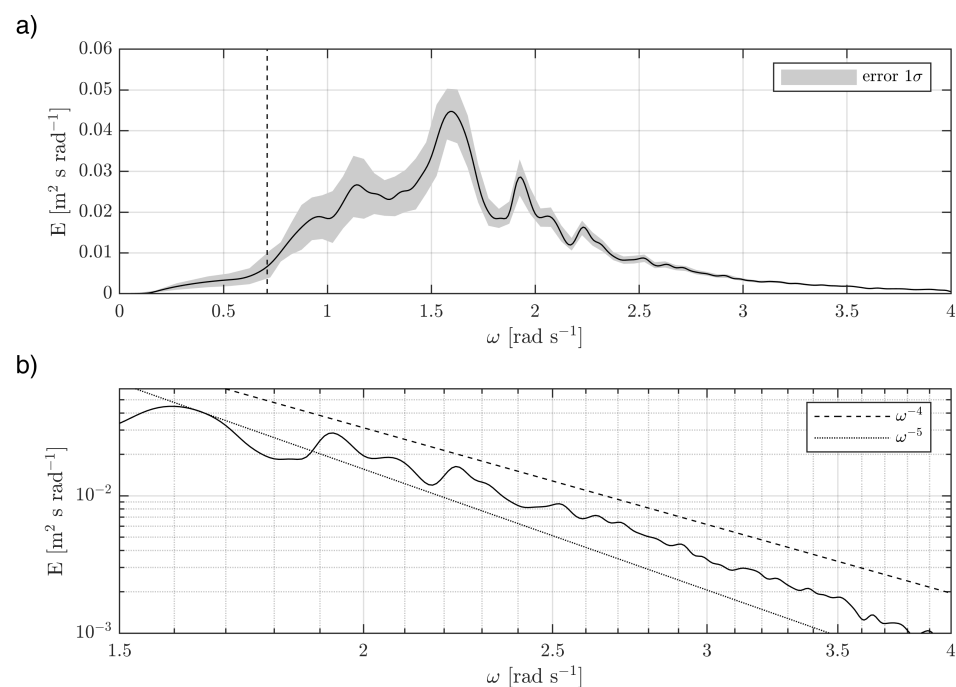


**Figure 2.** In (a), an exemplaric omnidirectional variance density spectrum with the  $1\sigma$ -error area indicated in grey is shown. The measurement was taken on 5 May 2020 close to Westerland at 12:50 UTC. Subfigure (b) shows the high frequency tail with logarithmic axes.

The high frequency tail slope follows the slope  $w^{-4} \dots w^{-5}$  as e.g., shown in [40]. This indicates a low impact of aliasing effects and the folding of energy of wavenumbers above the Nyquist frequency into wavenumbers below the Nyquist frequency. Due to the well known high-frequency tail slopes, the aliasing effect can be assumed to be neglectable.

The dotted line in Figure 2 indicates a lower limit of the measurements, since the scanned surface width of  $\approx 60\text{--}80\text{ m}$  does not allow interpretation below angular frequencies of around  $0.75\text{ rad s}^{-1}$ . In future measurement setups, a wider swath width for an improved spectrum estimation (both omni- and two-dimensional) around the most frequently observed wave spectrum peaks would be preferable.

#### 4. Exemplaric Situation and Its Boundary Conditions

The flight analysed in this article took place on 8 August 2017 in the afternoon from 13:06–17:06 UTC (labelled as flight number 31 in [6,7]). It was performed from the airport Jade–Weser in Wilhelmshaven, Germany, ICAO code EDWI. The flight pattern is shown on the map in Figure 3 together with the bathymetry. The flight was conducted above complex bathymetry with significantly varying water depth along each flight leg.

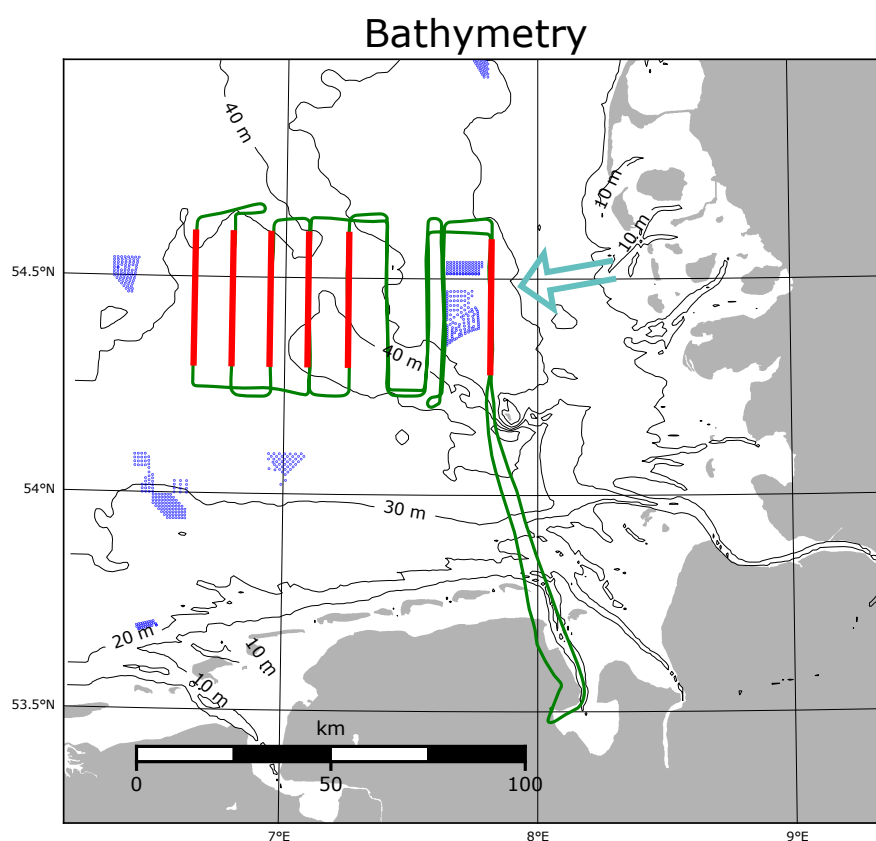


**Figure 3.** Map of the German Bight of the North Sea. Land areas are indicated in gray. The lines show bathymetry with 10, 20, 30, and 40 m isobaths. Wind turbines in operation in August 2017 are each shown as blue asterisks. The flight pattern is given as a green line, and the horizontal flight legs used in the laser scanner analyses are indicated as red lines. The arrow in light blue indicates the wind direction.

The horizontal flight legs were oriented in the North–South direction, parallel to the straight western edge of the wind park cluster officially termed N4, and were performed at hub height (constant altitude of 90 m). Several vertical profiles from 30 to 950 m altitude ASL were included North and South of the parallel legs.

The mean wind direction at hub height was  $80^\circ$ , and the mean wind speed was  $14\text{ m s}^{-1}$ . As warm wind was advected from land over the colder air masses, a strong



temperature inversion was present. The virtual potential temperature was 20.1 °C at the water surface and 22.0 °C at hub height [8]. Therefore, the atmosphere was stably stratified. As consequence, a long ranging downstream wind speed deficit, called a wake, was observed. The wake recovery of this particular case has been discussed from a meteorological point of view in Platis et al. [5] and Cañadillas et al. [8].

Despite the high wind speed at hub height, the near-surface wind speed was significantly reduced due to friction forces, which do not have an influence on higher altitudes due to the decoupling by the temperature inversion. Airborne measurements at the lowest altitudes of 30 m ASL showed a wind speed of around 9 m s<sup>-1</sup>. Numerical model data of the German Weather Service (DWD) showed a variable wind speed at 10 m altitude with an east component of around 4–7 m s<sup>-1</sup>.

Concerning the sea state, the situation was duration and fetch-limited. Due to the airflow around and between the wind parks (flow continuity), no completely undisturbed area was measured (compare Figure 4).

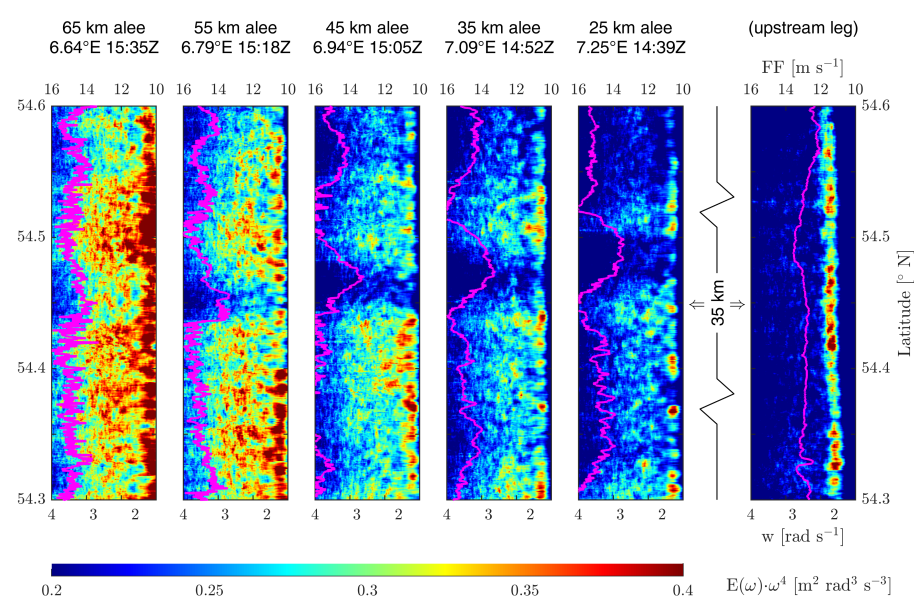


**Figure 4.** Sea surface energy distribution (variance density multiplied with  $\omega^4$ , colour coded) for the flight downstream of the wind park cluster N4 on 8 August 2017 with wind direction from the East. The wind speed measured at hub height is represented as an overlay in magenta.

## 5. Measured Spectra

Figure 4 shows the spectral energy distribution along the flight legs indicated in Figure 3 in colour coding and the wind speed at hub height as a magenta curve. The wind speed measured at the upstream leg (Figure 4, right panel) was around 12–14 m s<sup>-1</sup>. The variability can be induced by coastal effects. For all other legs measured at a distance of 25, 35, 45, 55, and 65 km downstream of the wind parks, the wind speed was visibly reduced, in particular in the wake of the most densely built wind park Amrumbank West. As the wind direction was 80°, the location of the wake with reduced wind speed was transferred southward for each flight leg (from right to left in Figure 4).

The spectrogram shows the development of the wave energy with increasing fetch. The fetch from land to the wind farm was roughly 35 km. The most western leg was about 100 km from shore. The spectra upstream of the windpark showed a quite homogeneous distribution of energy. The only notable variation was an increased peak energy around the latitude of the gap between the two wind parks and at the northern and southern edges. The spectra downstream showed a pronounced decrease of energy, in particular, inside the wake of the northern wind park, which is characterised by a much denser installation of wind turbines. Differences for areas influenced by the wake and not influenced are also

visible in Figure 5, where 1-D spectra are plotted inside and outside the wake at different downstream distances.

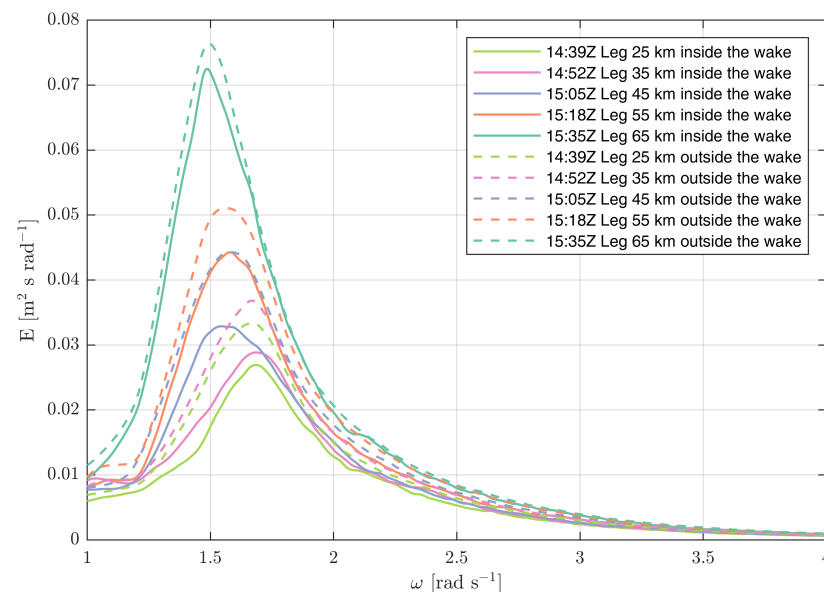


**Figure 5.** Variance density spectra inside and outside the wake. The general accordance with wave growth theory is evident, and a reduction of energy inside the wake is visible compared to the wave energy outside the wake in a relatively undisturbed area. The relative reduction in energy is shown in Figure 6.

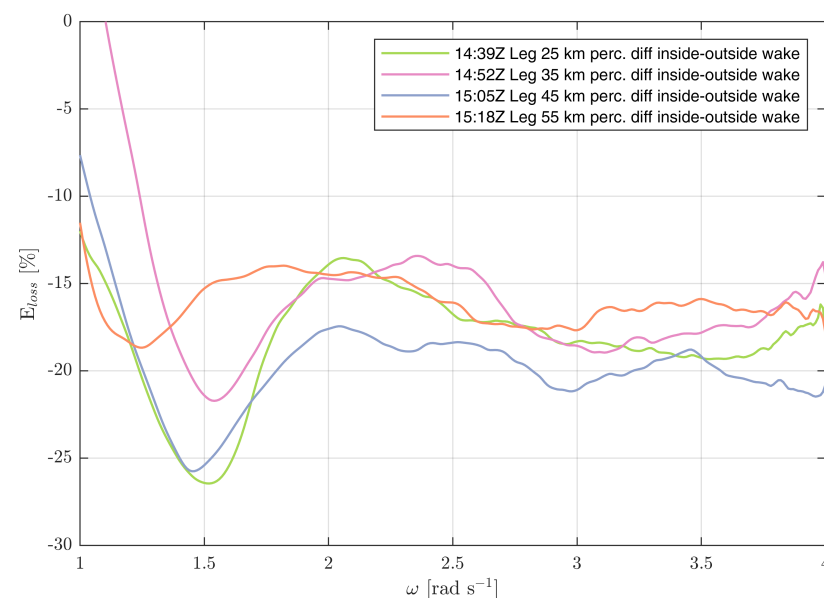


**Figure 6.** Relative wave energy reduction within the wake compared to the area outside the wake. The reduction is shown as a percent for the legs with a distance of 25, 35, 45, and 55 km behind the wind farm. Above  $2 \text{ rad s}^{-1}$ , the mean relative reduction in the wave energy is around 15–20 %, whereas the most significant reduction in energy is visible around the wave peaks.

The general ocean wave dynamics in this situation can, in a first approximation, be described by empirical relationships, which have been derived by other groups in previous studies. Examples are the Bjerkaas and Riede spectrum [41], the Donelan spectrum [42], or the Elfouhaily spectrum [43]. In this study, the parametric JONSWAP spectrum [44] was used. One reason for this choice was the fact that this empirical spectrum was originally



derived from a measurement campaign conducted less than 50 km north of the observations discussed here [44].

The respective JONSWAP experiment took place long before offshore windfarm installations began in the area and, thus, provides a good reference. As the observations were taken in a growing wind sea situation, the JONSWAP shape parameters were chosen as  $\gamma = 3.3$ ,  $\sigma_a = 0.07$ , and  $\sigma_b = 0.09$  in accordance with previous studies (e.g., [45]). The peak frequency  $\omega_p$  for a given wind speed at 10 m altitude  $U_{10}$  and a distance from the shoreline (fetch) can be estimated as

$$\omega_p \approx 22 \left( \frac{g^2}{U_{10} F} \right)^{1/3}. \quad (8)$$

The observed peak frequency of  $1.5 \text{ rad s}^{-1}$  is slightly higher than the empirical value range of  $1.14\text{--}1.27 \text{ rad s}^{-1}$ ; however, this can also be due to the temporal wind variability. The corresponding empirical JONSWAP spectra are shown in Figure 1 with an assumed scaling wind speed of  $3 \text{ m s}^{-1}$  (dashed lines) and  $4 \text{ m s}^{-1}$  (solid lines), according to common wind profiles in a stably stratified MABL (marine atmospheric boundary layer) assuming  $U_{hub height} \approx 9 \text{ m s}^{-1} \dots 14 \text{ m s}^{-1}$ . The observed and the empirical spectra are in reasonably good agreement in terms of both the energy and peak frequencies, which means that the observations are consistent with general wave theory. A comparison of the peak frequencies and the significant wave heights outside of the wake area are given in Table 1. In addition, this table contains the respective values derived from the spectra inside the wake.

**Table 1.** Significant wave heights as measured by the scanning laser and predicted by the empirical JONSWAP spectrum. The given values refer to different downstream distances to the offshore windfarm.

Distance to OWF	Observation $H_s$ [m]		JONSWAP $H_s$ [m]	
	Inside	Outside	3 m/s	4 m/s
25 km	0.64	0.70	0.54	0.70
35 km	0.68	0.72	0.59	0.77
45 km	0.71	0.80	0.64	0.83
55 km	0.77	0.82	0.69	0.89
65 km	0.92	0.94	0.73	0.94

Another interesting feature visible in Figure 5 is a slight dip in the spectra around a frequency of about  $2 \text{ rad s}^{-1}$ . This is roughly the peak frequency expected for the location of the wind park (see Figure 1). This is also consistent with the peak frequency observed by the laser that was upstream close to the wind park (see Figure 4). The energy for frequencies below  $2 \text{ rad s}^{-1}$  appears to be slightly reduced in the observations. This can be explained by the shape of the wind source function  $S_{wind}$  in Equation (1), which has most of the wind energy into the spectral regime around the peak of the spectrum [22]. This means that, downstream of the windpark, the spectral regime below  $2 \text{ rad s}^{-1}$  received less energy from the wind, due to the atmospheric wake.

The relative reduction in energy is shown in Figure 6. Above  $2 \text{ rad s}^{-1}$ , the mean relative reduction in wave energy is around 15–20 %, whereas the most significant reduction in energy is visible around the wave peaks. This is likely associated with nonlinear interactions. Since the measured situation outside the distinct wake of the windfarm Amrumbank West is influenced by the less dense windfarms Meerwind Süd/Ost and Nordsee Ost, further studies must be conducted to increase the statistical base.

## 6. Importance and Discussion of the Observations

In this study, the postulated impact of offshore wind farms on wave energy was proven and spectrally quantified for the first time with sea surface measurements. Although the measurements were taken in limited fetch and limited time conditions, the peak frequencies and wave energies are generally in accordance with wave theory concerning

wave growth. The general increase of wave height from north to south, as evident in Figure 4 by the increasing energy distribution, could be induced by the coastline and, therefore, the associated fetch length differences, see Figure 3.

A reduction in wave energy as theoretically examined with an extension of around 15 km in [21] was found to be evident up to 55 km downwind of the offshore wind park. The retrieved spectral features—which are likely connected to four wave interactions, see e.g., [46]—should be analysed in more detail in the future to enable the implementation of bidirectional coupling between the atmosphere and the sea state around offshore wind farms in wave models. The study of waves around offshore wind farms is of practical relevance and can potentially improve our understanding of wave physics.

An improved understanding of wave physics in complex areas, like the German Bight, is of interest for investigations regarding the influence of structures in coastal areas and their influence on the wind–wave climate, hydrodynamics, and ultimately the biosphere and sea life.

**Author Contributions:** K.B. performed the laser scanner data processing, spectra analysis and visualisation. J.S.-S. calculated the theoretical spectra and contributed to the interpretation of the spectra. A.L. contributed to the meteorological analysis. All authors contributed to the text writing, reviewing results, and editing. All authors have read and agreed to the published version of the manuscript.

**Funding:** Measurements used in this research were part of the project WIPAFF, which was funded by the Federal Ministry for Economic Affairs and Energy under grant number 0325783. We acknowledge support by the German Research Foundation and the Open Access Publication Funds of Technische Universität Braunschweig.

**Data Availability Statement:** The meteorological data of the WIPAFF measurements are publicly available at [6]. The large laser scanner raw data set is available upon request.

**Acknowledgments:** The authors would like to thank the WIPAFF partners for the great collaboration in this project, Stefan Emeis, Simon Siedersleben, Thomas Neumann, Beatriz Canadillas, Jens Bange, Andreas Platis, and Bughsin Djath. Further, the authors would like to thank the aircraft crew for the flights and the data acquisition above the North Sea, Rolf Hankers, Thomas Feuerle, Mark Bitter, Helmut Schulz, and Thomas Rausch.

**Conflicts of Interest:** The authors declare no conflict of interest. The funders had no role in the design of the study; in the collection, analyses, or interpretation of data; in the writing of the manuscript, or in the decision to publish the results.

## References

1. Piria, R.; Magosch, M.; Eckardt, J. *Offshore Wind Deployment in Germany*; Adelphi Consult GMBH: Berlin, Germany, 2020.
2. Christiansen, M.B.; Hasager, C.B. Wake Effects of Large Offshore Wind Farms Identified from Satellite SAR. *Remote Sens. Environ.* **2005**, *98*, 251–268. [\[CrossRef\]](#)
3. Djath, B.; Schulz-Stellenfleth, J.; Cañadillas, B. Impact of Atmospheric Stability on X-Band and C-Band Synthetic Aperture Radar Imagery of Offshore Windpark Wakes. *J. Renew. Sustain. Energy* **2018**, *10*, 043301. [\[CrossRef\]](#)
4. Djath, B.; Schulz-Stellenfleth, J. Wind Speed Deficits Downstream Offshore Wind Parks—A New Automated Estimation Technique Based on Satellite Synthetic Aperture Radar Data. *Meteorol. Z.* **2019**, 499–515. [\[CrossRef\]](#)
5. Platis, A.; Bange, J.; Bärfuss, K.; Cañadillas, B.; Hundhausen, M.; Djath, B.; Lampert, A.; Schulz-Stellenfleth, J.; Siedersleben, S.; Neumann, T.; Emeis, S. Long-Range Modifications of the Wind Field by Offshore Wind Parks—Results of the Project WIPAFF. *Meteorol. Z.* **2020**. [\[CrossRef\]](#)
6. Bärfuss, K.; Hankers, R.; Bitter, M.; Feuerle, T.; Schulz, H.; Rausch, T.; Platis, A.; Bange, J.; Lampert, A. *In-Situ Airborne Measurements of Atmospheric and Sea Surface Parameters Related to Offshore Wind Parks in the German Bight*; PANGAEA: Published Online, 2019. [\[CrossRef\]](#)
7. Lampert, A.; Bärfuss, K.; Platis, A.; Siedersleben, S.; Djath, B.; Cañadillas, B.; Hunger, R.; Hankers, R.; Bitter, M.; Feuerle, T.; et al. In Situ Airborne Measurements of Atmospheric and Sea Surface Parameters Related to Offshore Wind Parks in the German Bight. *Earth Syst. Sci. Data* **2020**, *12*, 935–946. [\[CrossRef\]](#)
8. Cañadillas, B.; Foreman, R.; Barth, V.; Siedersleben, S.; Lampert, A.; Platis, A.; Djath, B.; Schulz-Stellenfleth, J.; Bange, J.; Emeis, S.; Neumann, T. Offshore Wind Farm Wake Recovery: Airborne Measurements and Its Representation in Engineering Models. *Wind Energy* **2020**, *23*, 1249–1265. [\[CrossRef\]](#)

9. Siedersleben, S.K.; Platis, A.; Lundquist, J.K.; Lampert, A.; Bärfuss, K.; Cañadillas, B.; Djath, B.; Schulz-Stellenfleth, J.; Bange, J.; Neumann, T.; Emeis, S. Evaluation of a Wind Farm Parametrization for Mesoscale Atmospheric Flow Models with Aircraft Measurements. *Meteorol. Z.* **2018**, 401–415. [\[CrossRef\]](#)
10. Siedersleben, S.K.; Lundquist, J.K.; Platis, A.; Bange, J.; Bärfuss, K.; Lampert, A.; Cañadillas, B.; Neumann, T.; Emeis, S. Micrometeorological Impacts of Offshore Wind Farms as Seen in Observations and Simulations. *Environ. Res. Lett.* **2018**, 13, 124012. [\[CrossRef\]](#)
11. Siedersleben, S.K.; Platis, A.; Lundquist, J.K.; Djath, B.; Lampert, A.; Bärfuss, K.; Cañadillas, B.; Schulz-Stellenfleth, J.; Bange, J.; Neumann, T.; Emeis, S. Turbulent Kinetic Energy over Large Offshore Wind Farms Observed and Simulated by the Mesoscale Model WRF (3.8.1). *Geosci. Model Dev.* **2020**, 13, 249–268. [\[CrossRef\]](#)
12. Platis, A.; Siedersleben, S.K.; Bange, J.; Lampert, A.; Bärfuss, K.; Hankers, R.; Cañadillas, B.; Foreman, R.; Schulz-Stellenfleth, J.; Djath, B.; Neumann, T.; Emeis, S. First in Situ Evidence of Wakes in the Far Field behind Offshore Wind Farms. *Sci. Rep.* **2018**, 8, 2163. [\[CrossRef\]](#)
13. Bärfuss, K.; Djath, B.; Lampert, A.; Schulz-Stellenfleth, J. Airborne LiDAR Measurements of Sea Surface Properties in the German Bight. *IEEE Trans. Geosci. Remote Sens.* **2020**, 1–10. [\[CrossRef\]](#)
14. Karyotakis, A. On the Optimisation of Operation and Maintenance Strategies for Offshore Wind Farms. Ph.D. Thesis, University College London, London, UK, 2011.
15. Staneva, J.; Alari, V.; Breivik, Ø.; Bidlot, J.R.; Mogensen, K. Effects of Wave-Induced Forcing on a Circulation Model of the North Sea. *Ocean Dyn.* **2017**, 67, 81–101. [\[CrossRef\]](#)
16. Fischereit, J.; Larsén, X. G. Relevance of Sea Waves and Farm-Farm Wakes for Offshore Wind Resource Assessment. In Proceedings of the EERA DeepWind Conference, Trondheim, Norway, 15–17 January 2020.
17. Broström, G. On the Influence of Large Wind Farms on the Upper Ocean Circulation. *J. Mar. Syst.* **2008**, 74, 585–591. [\[CrossRef\]](#)
18. Paskyabi, M.B. Offshore Wind Farm Wake Effect on Stratification and Coastal Upwelling. *Energy Procedia* **2015**, 80, 131–140. [\[CrossRef\]](#)
19. van Berkel, J.; Burchard, H.; Christensen, A.; Mortensen, L.; Petersen, O.; Thomsen, F. The Effects of Offshore Wind Farms on Hydrodynamics and Implications for Fishes. *Oceanography* **2020**, 33, 108–117. [\[CrossRef\]](#)
20. Ponce de León, S.; Bettencourt, J.H.; Kjerstad, N. Simulation of Irregular Waves in an Offshore Wind Farm with a Spectral Wave Model. *Cont. Shelf Res.* **2011**, 31, 1541–1557. [\[CrossRef\]](#)
21. Christensen, E.D.; Johnson, M.; Sørensen, O.R.; Hasager, C.B.; Badger, M.; Larsen, S.E. Transmission of Wave Energy through an Offshore Wind Turbine Farm. *Coast. Eng.* **2013**, 82, 25–46. [\[CrossRef\]](#)
22. Komen, G.J.; Cavaleri, L.; Donelan, M.; Hasselmann, K.; Hasselmann, S.; Janssen, P.A.E.M. *Dynamics and Modelling of Ocean Waves*; Cambridge University Press: Cambridge, UK, 1996.
23. Corsmeier, U.; Hankers, R.; Wieser, A. Airborne Turbulence Measurements in the Lower Troposphere Onboard the Research Aircraft Dornier 128–6. D-IBUF. *Meteorol. Z.* **2001**, 315–329. [\[CrossRef\]](#)
24. Reineman, B.D.; Lenain, L.; Castel, D.; Melville, W.K. A Portable Airborne Scanning Lidar System for Ocean and Coastal Applications. *J. Atmos. Ocean. Technol.* **2009**, 26, 2626–2641. [\[CrossRef\]](#)
25. Walsh, E.J.; Iii, D.W.H.; Hines, D.E.; Swift, R.N.; Scott, J.F. Wave-Measurement Capabilities of the Surface Contour Radar and the Airborne Oceanographic Lidar. *John Hopkins APL Tech. Dig.* **1987**, 13, 74–81.
26. Melville, W.; Lenain, L.; Romero, L.; Statom, N. Airborne Lidar in Support of Ocean Topography Missions and Science. In Proceedings of the 20 Years of Progress in Radar Altimetry, Venice, Italy, 24–29 September 2012.
27. Romero, L.; Melville, W.K. Airborne Observations of Fetch-Limited Waves in the Gulf of Tehuantepec. *J. Phys. Oceanogr.* **2010**, 40, 441–465. [\[CrossRef\]](#)
28. Schwithal, A.; Tonhäuser, C.; Wolkow, S.; Angermann, M.; Hecker, P.; Mumm, N.; Holzapfel, F. Integrity Monitoring in GNSS/INS Systems by Optical Augmentation. In Proceedings of the 2017 DGON Inertial Sensors and Systems (ISS), Karlsruhe, Germany, 19–20 September 2017; pp. 1–22. [\[CrossRef\]](#)
29. Herbers, T.H.C.; Jessen, P.F.; Janssen, T.T.; Colbert, D.B.; MacMahan, J.H. Observing Ocean Surface Waves with GPS-Tracked Buoys. *J. Atmos. Ocean. Technol.* **2012**, 29, 944–959. [\[CrossRef\]](#)
30. Holthuijsen, L.H. *Waves in Oceanic and Coastal Waters*; Cambridge University Press: Cambridge, UK, 2007. [\[CrossRef\]](#)
31. Otremba, Z.; Piskozub, J. Modelling the Bidirectional Reflectance Distribution Function (BRDF) of Seawater Polluted by an Oil Film. *Opt. Express* **2004**, 12, 1671–1676. [\[CrossRef\]](#) [\[PubMed\]](#)
32. Sayer, A.M.; Thomas, G.E.; Grainger, R.G. A Sea Surface Reflectance Model for (A)ATSR, and Application to Aerosol Retrievals. *Atmos. Meas. Tech.* **2010**, 3, 813–838. [\[CrossRef\]](#)
33. Nyquist, H. Certain Topics in Telegraph Transmission Theory. *Proc. IEEE* **2002**, 90, 280–305. [\[CrossRef\]](#)
34. Wehr, A.; Lohr, U. Airborne Laser Scanning—an Introduction and Overview. *ISPRS J. Photogramm. Remote Sens.* **1999**, 54, 68–82. [\[CrossRef\]](#)
35. Walsh, E.J.; Hancock, D.W.; Hines, D.E.; Swift, R.N.; Scott, J.F. Directional Wave Spectra Measured with the Surface Contour Radar. *J. Phys. Oceanogr.* **1985**, 15, 566–592. [\[CrossRef\]](#)
36. Young, I.R. *Wind Generated Ocean Waves*, 1st ed.; Elsevier Ocean Engineering Book Series; Elsevier Science Ltd.: Kidlington, UK, 1999; Volume 2.

- 
37. Lenain, L.; Melville, W.K. Measurements of the Directional Spectrum across the Equilibrium Saturation Ranges of Wind-Generated Surface Waves. *J. Phys. Oceanogr.* **2017**, *47*, 2123–2138. [[CrossRef](#)]
  38. Plant, W.J.; Keller, W.C.; Hayes, K. Simultaneous Measurement of Ocean Winds and Waves with an Airborne Coherent Real Aperture Radar. *J. Atmos. Ocean. Technol.* **2005**, *22*, 832–846. [[CrossRef](#)]
  39. Long, R.B. On Surface Gravity Wave Spectra in a Moving Frame of Reference. In *NOAA Technical Memorandum ERL AOML 38*; Atlantic Oceanographic and Meteorological Laboratories: Miami, FL, USA, 1979.
  40. Leckler, F.; Ardhuin, F.; Peureux, C.; Benetazzo, A.; Bergamasco, F.; Dulov, V. Analysis and Interpretation of Frequency–Wavenumber Spectra of Young Wind Waves. *J. Phys. Oceanogr.* **2015**, *45*, 2484–2496. [[CrossRef](#)]
  41. Bjerkaas, A.; Riedel, F. *Proposed Model for the Elevation Spectrum of a Wind-Roughened Sea Surface*; Technical Report; Johns Hopkins University, Applied Physics Laboratory: Laurel, MD, USA, 1979.
  42. Donelan, M.A.; Pierson Jr, W.J. Radar scattering and equilibrium ranges in wind-generated waves with application to scatterometry. *J. Geophys. Res. Ocean.* **1987**, *92*, 4971–5029. [[CrossRef](#)]
  43. Elfouhaily, T.; Chapron, B.; Katsaros, K.; Vandemark, D. A unified directional spectrum for long and short wind-driven waves. *J. Geophys. Res. Ocean.* **1997**, *102*, 15781–15796. [[CrossRef](#)]
  44. Hasselmann, K.; Barnett, T.P.; Bouws, E.; Carlson, H.; Cartwright, D.E.; Enke, K.; Ewing, J.A.; Gienapp, H.; Hasselmann, D.E.; Kruseman, P.; et al. Measurements of Wind-Wave Growth and Swell Decay during the Joint North Sea Wave Project (JONSWAP). *Ergänzungsheft Dtsch. Hydrogr. Z. Reihe A* **1973**, *8*, 12.
  45. Brüning, C.; Alpers, W.; Hasselmann, K. Monte-Carlo simulation studies of the nonlinear imaging of a two dimensional surface wave field by a synthetic aperture radar. *Remote Sens.* **1990**, *11*, 1695–1727. [[CrossRef](#)]
  46. Janssen, P. *The Interaction of Ocean Waves and Wind*; Cambridge University Press: Cambridge, UK, 2004. [[CrossRef](#)]